Supporting Information

Bayrhuber *et al.* 10.1073/pnas.0808115105

SI Text

Preparation of Functional hVDAC1. Expression, refolding and purification of hVDAC1 were done mostly as described in ref. 1. Opposite to our previous studies, we attached a His-6-Tag to the C terminus of hVDAC1 that improved the overall folding properties of the protein (data not shown). The homogeneity of the protein was determined by size exclusion chromatography (data not shown). The pore forming activity was confirmed by reconstitution of hVDAC1 in planar bilayer membranes and subsequent measurement of membrane currents as described in ref. 1.

Site-Directed Mutagenesis. Point mutations were introduced with the QuikChange site-directed mutagenesis kit (Stratagene), which was used essentially as recommended by Stratagene. Successful mutagenesis was verified by DNA sequence analysis.

NMR Spectroscopy. 3D spectra were recorded from a perdeuterated $^{15}N/^{13}C$ labeled sample containing 0.6 mM HVDAC, 25 mM BisTris, approx. 250 mM Lauryldimethylamine-oxide (LDAO), 10% D_2O, pH 6.8. All spectra were measured at 37°C on either Bruker 600, 800 or 900 MHz spectrometers equipped with cryogenic probeheads. Three different TROSY-type triple resonance experiments were recorded: HNCA, HNCO and multiple quantum (mq) HNCOCA (provided by R. Riek). In addition, ^{15}N-edited ^{1}H-^{1}H NOESY-TROSY (2) spectra and mixed-time parallel evolution HMQC-NOESY (3) spectra were recorded on samples with varying deuteration levels:

(*i*) ^{15}N-NOESY-TROSY on $^{2}H(99\%)/^{13}C/^{15}N$ hVDAC1 (94 × 20x512 points in the t1,t2, and t3 domain; 32 transients; mixing time of 160 ms; 800 MHz NMR spectrometer with cryo probe).

(*ii*) ^{15}N-NOESY-TROSY on $^{2}H(75\%)/^{15}N$ hVDAC1 (60 × 25 × 512 points in the t1,t2, and t3 domain; 48 transients; mixing time of 100 ms; 900 MHz NMR spectrometer with cryo probe)

(*iii*) ^{15}N-NOESY-TROSY on $^{2}H(75\%)/^{15}N$ hVDAC1in 100% D_2O (53 × 25 × 512 points in the t1,t2, and t3 domain; 48 transients; mixing time of 180 ms; 900 MHz NMR spectrometer with cryoprobe.

(*iv*) ^{15}N-NOESY-TROSY on $^{2}H(50\%)/^{15}N$ hVDAC1 (107 × 19 × 512 points in the t1,t2, and t3 domain; 32 transients; mixing time of 90 ms; 900 MHz NMR spectrometer with cryo probe).

Further spectra were recorded on VDAC mutants:

(*v*) ^{15}N-NOESY-HMQC on $^{2}H(75\%)/^{15}N$-C232SV17C hVDAC1 (91 × 25 × 512 points in the t1,t2, and t3 domain; 26 transients; mixing time of 120 ms; 800 MHz spectrometer with cryoprobe.

(*vi*) ^{15}N-NOESY-HMQC on $^{2}H(75\%)/^{15}N$-E73V hVDAC1 (85 × 25 × 512 points in the t1,t2,and t3 domain; 26 transients; mixing time of 240 ms; 800 MHz spectrometer with cryoprobe).

(*vii*) ^{15}N-NOESY-HMQC on $^{2}H(75\%)/^{15}N$-C232SC127SV87C hVDAC1 (85 × 25 × 512 points in the t1,t2, and t3 domain; 26 transients; mixing time of 240 ms; 800 MHz spectrometer with cryoprobe).

The NMR data were processed and analyzed using NMRPipe, NMRDraw (4) and SPARKY (T. D. Goddard and D. G. Kneller, SPARKY 3, University of California, San Francisco).

Assignment of backbone resonance of hVDAC1 was achieved through six independent types of NMR data: Cα chemical shift connectivity, intra-strand and sequential HN-HN NOEs, amino acid specific labeling (^{2}H-hVDAC1-^{15}N-Met-$^{15}N/^{13}C$-Leu-$^{15}N/^{13}C$-Ile, ^{2}H-hVDAC1-$^{15}N/^{13}C$-Val, ^{2}H-hVDAC1-^{15}N-Tyr, ^{2}H-hVDAC1-^{15}N-Ala, ^{2}H-hVDAC1-^{15}N-Phe, ^{2}H-hVDAC1-^{15}N-Lys, ^{2}H-hVDAC1-^{15}N-Arg), 20 point mutations (E73V, C127S, C232S, C127SC232S, C232SV17C, C127SC232SL31C C127SC232SS43C, C127SC232SS46C, C127SC232ST49C, C127SC232SV54C, C127SC232ST60C, C127SC232ST65C, C127SC232ST72C, C127SC232SL81C, C127SC232SV87C, C127SC232SL97C, C127SC232SS193C, C127SC232SS260C, C127SC232SL277C and C127SC232SF281C), paramagnetic broadening induced by spin labels (using all single cysteine mutants listed above) and hydrogen/deuterium exchange experiments (using wild-type and E73V hVDAC1).

Backbone dynamics were studied by measuring steady state heteronuclear $^{15}N\{^{1}H\}$-NOEs employing the TROSY strategy (5). Heteronuclear NOE values are reported as the ratio of peak heights in paired spectra collected with and without an initial period (4 s) of proton saturation during the 5-s recycle delay. The global correlation time of the protein/micelle complex was estimated by recording a $^{15}N/^{1}H$-TRACT experiment (6). The rotational correlation time is determined to be 60 ns. This correlation time is expected to a solution of VDAC in micelles with a predominance of monomer and a minor population of dimer. This result is obtained by comparison with OmpX reconstituted in DHPC micelles. DHPC with two lipid chains and a molecular weight of 453 D corresponds to two LDAO molecules with only one lipid chain of molecular weight of 229 D. OmpX has a molecular weight of 16 kDa and has 8 β-strands in the barrel. Its correlation time is 21 ns in DHPC micelles corresponding to an overall molecular weight of approx. 50 kDa (11). The circumference of VDAC with 19 β-strands is 19/8 times larger than that of OmpX with 8 β-strands. At the same time, VDAC is approximately twice as heavy as OmpX yielding an expected molecular weight of 142 kDa which would render a rotational correlation time of ≈60 ns. This is the observed correlation time, which would be compatible with VDAC statically fixed in the micelle. If we allow for rotation of VDAC in the micelle, a smaller correlation time would result, that would then require presence of a minor amount of dimer. Thus, the correlation time is compatible with a monomer/dimer equilibrium with a predominance of the monomer in solution. It should be noted that the local concentration of VDAC in micelles is much lower than the local concentration of VDAC in the mitochondrial outer membrane which for potato tuber mitochondria was estimated to be 50 mM (7). Interestingly, this is also approximately the concentration of VDAC in the crystal.

The molecular weight observed in NMR is compatible with the molecular weight observed in gel filtration with Cymal-5 in which one observes one band at a molecular weight well over 100 kDa.

To identify solvent protected amide protons, $^{2}H/^{15}N$-labeled hVDAC1 and $^{2}H/^{15}N$-labeled E73V mutant hVDAC1 were lyophilised and subsequently dissolved in D_2O. Subsequently, series of 2D $^{1}H/^{15}N$ TROSY spectra were recorded.

Determination of Distance Restraints. Crosspeaks observed in 3D NOESY spectra (Table S1) were divided into three groups: strong, medium and weak. The corresponding distance restraint was set to 3 ± 1, 4 ± 1 and 5 ± 1 Å, respectively. In total, 95 unique HN-HN NOE distance restraints were extracted.

For measurement of paramagnetic relaxation enhancement, TROSY-HSQC spectra of two $^{2}H/^{15}N$-labeled hVDAC1 samples were recorded, one with and one without the paramagnetic MTSL-tag. Distance restraints were calculated as described from the peak intensity ratios (I_{para}/I_{dia}) of corresponding $^{15}N/^{1}H$

crosspeaks in the diamagnetic and paramagnetic states of the protein.[10] To reduce the impact of peak overlap, for each residue the average of its own intensity ratio I_{para}/I_{dia} and that of the preceding and following residue was calculated. These smoothed intensity ratios were linearly fit for the enhancement of the transverse relaxation rate by the unpaired electron (8, 9). For peaks broadened beyond detection, distances were restrained to a target value of 2.6 Å with limits of 0.0 to 10.0 Å. Peaks with intensity ratios below 0.95 were restrained to the calculated distance ± 5 Å. For residues that were not broadened in the paramagnetic state, a lower and upper distance bound of 15 and 100 Å, respectively, was used. All distances were imposed as restraints between the amide proton of the residue with the cysteine-MTSL group and residue-specific amide protons.

Normalized weighted average chemical shift changes induced by single-residue mutations were also converted into distance restraints. When the spectral quality was low, $\Delta\delta_{HN}$ values exceeding 0.04 ppm were translated into distance restraints of 15.0 ± 5 Å from the HN of the affected residue to the HN of the mutated residue. When the spectral quality was high, $\Delta\delta_{HN}$ values exceeding 0.05 ppm were translated into distance restraints of 5 Å with upper and lower bounds of 3 to 10 Å; $\Delta\delta_{HN}$ values between 0.038 and 0.05 ppm were converted into distance restraints of 15 ± 5 Å.

Distance restraints that localized the N-terminal helix are qualitatively summarized in Table S1.

Calculation of an Initial 3D Structural Model from NMR Data Used for Further X-Ray Refinement. An initial structural model was calculated with the Inferential Structure Determination (ISD) software (10) using experimental as well as theoretical restraints. The experimental NMR restraints comprised 95 NOEs between amide protons and dihedral angle restraints predicted from chemical shift data [368 backbone dihedral angles predicted with TALOS (11) and 170 side-chain dihedral angles predicted with SHIFTOR (12)]. The crystallographic data were used in the form of (*i*) positional restraints derived from the four selenomethionines that could be identified unambiguously, (*ii*) eight β strands that were manually built into the electron density map, (*iii*) the overall shape of the molecule as determined by the density-modified map and (*iv*) the location of the N-terminal helix visible in the electron density. In addition, the 2D topology (Figs. 1*B* and S1) defining β strands and their registers was encoded in 150 hydrogen bonds and 370 Cα-Cα distance restraints. The hydrogen bonds were derived based on the following reasoning: All pairs of β strands that are neighbors in sequence make up an anti-parallel β hairpin whose register is defined by one or more inter-strand NOEs. If an NOE is observed between residue i in one strand and residue j in a neighboring strand, this indicates that i and j are facing each other in the anti-parallel hairpin conformation implying that residues i and j form two hydrogen bonds: One in which the main-chain nitrogen atom of residue i is the donor and the backbone oxygen of j is the acceptor and vice versa. This results in four distance restraints in total, because a single hydrogen bond is defined by distance restraints between the donor and the acceptor and between the hydrogen and the acceptor. These restraints were established for all possible pairs of donors and acceptors i ± 2, j ± 2 that are part of the strands defined in the topology model. For β strands 19 and 1, parallel β strand restraints were derived in an analogous fashion. Additionally, Cα- Cα distance restraints were defined to stabilize the geometry of the strands. The pitch between two Cα atoms separated by n residues was n x 3.4 Å in β strands. We defined these restraints for all 19 strands letting *n* vary between 2 and 5.

All structure calculations were done with the ISD software using a standard replica exchange Monte Carlo setup to explore the conformational posterior distribution resulting from the experimental and theoretical constraints. The distance restraints were imposed using a lognormal distribution and the dihedral angles were modeled with a von Mises distribution. Only the main-chain and side-chain dihedral angles were sampled, bond lengths and bond angles were set to their ideal values.

Crystallographic Methods. Crystals of hVDAC1 were derived as described in Meins *et al.* (13). Crystallographic phasing was performed on the basis of one Se-methionine derivative and Pt-Derivatives. All data were integrated using the program XDS (14) and scaled using SCALA (15), taking special care to scale related datasets (e.g., from multiwavelength experiments) together to maximize the anomalous signal. The initial coordinates of Se positions were determined using SHELXD (16) and subsequently refined using first autoSHARP (17) and finally SHARP (18). Heavy atom sites in Pt derivatives were found using log-likelihood gradient maps as implemented in SHARP. The first set of experimental phases was improved using real-space density modification methods in programs SOLOMON (19) and DM (20). Several slightly different protocols were used, with only few of those leading to an initial map that showed a clear, low-resolution picture of the barrel. This is probably due to the very weak phasing power of the different datasets, the degree of non-isomorphism between them and the significant level of anisotropy the diffraction data of all crystals showed.

The Se sites of the various mutants refined in SHARP to occupancies between 1.0 and 2.0. Given the low resolution of the data, no absolute scale (based on a Wilson plot) can be obtained and these values have to be taken as relative occupancies. The B-factors of Se atoms were in the range of 200–300 Å. No other significant peaks were observed in anomalous Fourier maps or log-likelihood gradient maps as implemented in SHARP. The unambiguous placement of those Se-MET residues allowed the location of the correct barrel position. Since a beta-barrel is a very symmetrical object, and VDAC also shows no difference in inner and outer loop length, a placement of the correct sequence would have otherwise been impossible. One Se-MET mutation was in the N-terminal helix and allowed the placement of this structural element, too.

Map interpretation was started by placing fragments of high-resolution beta barrel protein structures (PDB ID 1PRN, 2F1C) in B-factor sharpened (21) electron density maps. Subsequent placement of further beta-sheets and iterative model building and geometry refinement was performed with O (22) and COOT (23), respectively.

The refinement of models within BUSTER-TNT (24) required the setting of various scale parameters (especially for the bulk-solvent contribution) to fixed values. These values were chosen to optimize the agreement between observed and calculated structure factor amplitudes. Initially, only the positions of rigid bodies were allowed to be refined–with the size of rigid bodies slowly decreasing from the whole molecule to separate secondary structure elements and loops. After including a full set of distance restraints (25) (for the N-O distance within parallel and anti-parallel beta-sheets and the N-O^{+3}/N-O^{+4} distances in alpha helices), individual positions and grouped B-factors were refined.

Similar to previously reported practices when refining low-resolution structures (21), the following specific techniques were used:

- Experimental phase information as obtained by SHARP in form of Hendrickson-Lattmann coefficients was used throughout the refinement
- Grouped B-factor refinement: one B-factor each for residues in beta-sheets, the N-terminal helix or loops.

- Secondary structure restraints between beta-strands were used (restraining N-O distances to 2.89 Å and 2.95 Å (25) for anti-parallel and parallel beta sheets respectively).
- The bulk solvent scaling model in BUSTER-TNT was not refined, but fixed at sensible values (k = 1.0 and B = 180). Leaving those parameters free to refine gave rise to unstable refinements, resulting in much higher R-factors and nonsensical scale parameters (B = 999.0 or k = 0), an experience similar to that observed in CNS (21).

The refined B-factors are 165 Å^2 for the N-terminal helix, 150 Å^2 for the β barrel and 216 Å^2 for loop regions. These values seem very high, but one has to consider the low resolution and anisotropy of the data. Together with the observation that most of the datasets measured show severe non-isomorphism relative to each other these seem a reasonable range of values. Furthermore, an analysis of the average B-factor of low-resolution structures (between 3.9 and 5.0 Å) deposited in the PDB as of July 24, 2008, shows a range of values between 0.53 Å and 271.81 Å^2 with a mean of 91 Å^2 and a sigma of 66 Å^2. This average value for deposited structures seems even on the low side, since several of these low-resolution structures have their B-factors fixed at surprisingly low values of 10 or 20 Å^2.

Due to the very small number of reflections (4,840 in the range 25–4.1 Å) - leading to a small set of test reflections (477) - the statistical indicators in various resolution shells suffer from the small numbers of reflections contributing to them. This might explain the unusual trend in R(work) and R(test) decreasing with resolution (Table S3). Looking at deposited structures in the PDB (between 3.9 and 5.0 Å) as of July 24, 2008, it does not seem to be that uncommon: out of the 54 entries which have R(work) and R(test) reported for both overall and highest resolution bin, 11 show at least one of R-factor to be lower in the highest resolution bin than for the overall resolution range.

An R_{free} of 38.7% is not that unusually high considering the fact that no predetermined crystal structure could be used (for molecular replacement) and no non-crystallographic symmetry was present (to increase the observation-parameter ratio during refinement as well as giving much better initial electron density through averaging in density modification). To illustrate this, an analysis of deposited PDB structures was done. As of July 24, 2008, there are 170 PDB entries available with high resolution limits between 3.9 and 5.0 Å. Those 170 were analyzed according to date of data collection, date of deposition, overall R-factors (working and test set), overall completeness, low and high resolution limit, B-factors (from Wilson plot and model), F/sigma cutoff during refinement, presence of NCS, method of structure solution.

- 114 entries stated "molecular replacement," "Fourier synthesis" or similar as the method for structure solution; 13 of those didn't have values for both R-factors (working and test set). The remaining 101 entries have
  · R(work) : <mean> = 0.2874 with sd = 0.0584
  · R(test) : <mean> = 0.3283 with sd = 0.0531.
- Using only structures for which data were collected in 2000 or later: 75 entries stated "molecular replacement," "Fourier synthesis" or similar as the method for structure solution. 3 of those didn't have values for both R-factors (working and test set). The remaining 72 entries give
  ·R(work) : <mean> = 0.2851 with sd = 0.0517
  ·R(test) : <mean> = 0.3258 with sd = 0.0494.
- 25 entries are based on heavy-atom methods (SAD, MAD, SIR(AS) or MIR(AS)). 8 of those didn't have values for both R-factors (working and test set). The remaining 17 entries give
  ·R(work) : <mean> = 0.3368 with sd = 0.0476
  ·R(test) : <mean> = 0.3700 with sd = 0.0477.
- Using only structures for which data were collected in 2000 or later: 16 entries are based on heavy-atom methods [SAD, MAD, SIR(AS), or MIR(AS)]; 2 of those didn't have values for both R-factors (working and test set). The remaining 14 entries give
  ·R(work) : <mean> = 0.3298 with sd = 0.0495
  ·R(test) : <mean> = 0.3601 with sd = 0.0464.

This shows that refinement of low resolution structures from a very good starting model (as is usually the case for molecular replacement solutions), tend to give lower R-factors than structures based on experimental phasing. Our Rfree value of 0.387 is within 0.6 sigma of all experimentally phased structures deposited after 2000 in the resolution range 3.9–5.0 Å.

Furthermore, if one also discards all of those 14 structures that have noncrystallographic symmetry (leading to better observation-parameter ratio, better maps and better models), only three structures remain of which 2BF1 and 2QAG have a larger Rfree than our structure.

1. Engelhardt H, *et al.* (2007) High-level expression, refolding and probing the natural fold of the human voltage-dependent anion channel isoforms I and II. *J Membr Biol* 216:93–105.
2. Xia Y, Sze K, Zhu G (2000) Transverse relaxation optimized 3D and 4D 15n/15N separated NOESY experiments of 15N labeled proteins. *J Biomol NMR* 18:261–268.
3. Ying J, Chill JH, Louis JM, Bax A (2007) Mixed-time parallel evolution in multiple quantum NMR experiments: sensitivity and resolution enhancement in heteronuclear NMR. *J Biomol NMR* 37:195–204.
4. Delaglio F, *et al.* (1995) NMRPipe: A multidimensional spectral processing system based on UNIX pipes. *J Biomol NMR* 6:277–293.
5. Zhu G, Xia Y, Nicholson LK, Sze KH (2000) Protein dynamics measurements by TROSY-based NMR experiments. *J Magn Reson* 143:423–426.
6. Lee D, Hilty C, Wider G, Wuthrich K (2006) Effective rotational correlation times of proteins from NMR relaxation interference. *J Magn Reson* 178:72–76.
7. Hoogenboom BW, Suda K, Engel A, Fotiadis D (2007) The supramolecular assemblies of voltage-dependent anion channels in the native membrane. *J Mol Biol* 370:246–255.
8. Gillespie JR, Shortle D (1997) Characterization of long-range structure in the denatured state of staphylococcal nuclease. II. Distance restraints from paramagnetic relaxation and calculation of an ensemble of structures. *J Mol Biol* 268:170–184.
9. Battiste JL, Wagner G (2000) Utilization of site-directed spin labeling and high-resolution heteronuclear nuclear magnetic resonance for global fold determination of large proteins with limited nuclear Overhauser effect data. *Biochemistry* 39:5355–5365.
10. Rieping W, Habeck M, Nilges M (2005) Inferential structure determination. *Science* 309:303–306.
11. Cornilescu G, Delaglio F, Bax A (1999) Protein backbone angle restraints from searching a database for chemical shift and sequence homology. *J Biomol NMR* 13:289–302.
12. Neal S, Berjanskii M, Zhang H, Wishart DS (2006) Accurate prediction of protein torsion angles using chemical shifts and sequence homology. *Magn Reson Chem* 44 Spec No: 158–167.
13. Meins T, Vonrhein C, Zeth K (2008) Crystallization and preliminary X-ray crystallographic studies of human voltage-dependent anion channel isoform I (HVDAC1). *Acta Crystallogr F* 4:651–5.
14. Kabsch W (1993) Automatic processing of rotation diffraction data from crystals of initially unknown symmetry and cell constants. *J Appl Cryst* 26:795–800.
15. Collaborative (1994) The CCP4 suite: programs for protein crystallography. *Acta Crystallogr D* 50:760–763.
16. Sheldrick GM (2008) A short history of SHELX. *Acta Crystallogr A* 64:112–122.
17. Vonrhein C, Blanc E, Roversi P, Bricogne G (2006) Automated structure solution with autoSHARP. *Methods Mol Biol* 364:215–230.
18. Bricogne G, Vonrhein C, Flensburg C, Schiltz M, Paciorek W (2003) Generation, representation and flow of phase information in structure determination: recent developments in and around SHARP 2.0. *Acta Crystallogr D* 59:2023–2030.
19. Abrahams JP, Leslie AG (1996) Methods used in the structure determination of bovine mitochondrial F1 ATPase. *Acta Crystallogr D* 52:30–42.
20. Cowtan K, Main P (1998) Miscellaneous algorithms for density modification. *Acta Crystallogr D* 54:487–493.
21. De La Barre B, Brunger AT (2006) Considerations for the refinement of low resolution crystal structures. *Acta Crystallogr D* 62:923–932.
22. Jones TA, Zou JY, Cowan SW, Kjelgaard M (1991) Improved methods for building protein models in electron density maps and location of errors in these models. *Acta Crystallogr A* 47:110–119.
23. Emsley P, Cowtan K (2004) Coot: Model-building tools for molecular graphics. *Acta Crystallogr D* 60:2126–2132.

24. Roversi P, Blanc E, Vonrhein C, Evans G, Bricogne G (2000) Modelling prior distributions of atoms for macromolecular refinement and completion. *Acta Crystallogr D* 56:1316–1323.
25. Fabiola GF, Krishnaswamy S, Nagarajan V, Pattabhi V (1997) C-H.O hydrogen bonds in beta-sheets. *Acta Crystallogr D* 53:316–320.
26. Strong M, Sawaya MR, Wang S, Phillips M, Cascio D, Eisenberg D (2006) Toward the structural genomics of complexes: crystal structure of a PE/PPE protein complex from Mycobacterium tuberculosis. *Proc Natl Acad Sci USA* 103:80608–80665.
27. Chen B, *et al.* (2005). Structure of an unliganded simian immunodeficiency virus gp120 core. *Nature* 433:834–841.
28. Corbett KD, Benedetti P, Berger JM (2007). Holoenzyme assembly and ATP-mediated conformational dynamics of topoisomerase VI. *Nat Struct Mol Biol* 14:611–619.
29. Sirajuddin M, *et al.* (2007). Structural insight into filament formation by mammalian septins. *Nature* 449:311–315.

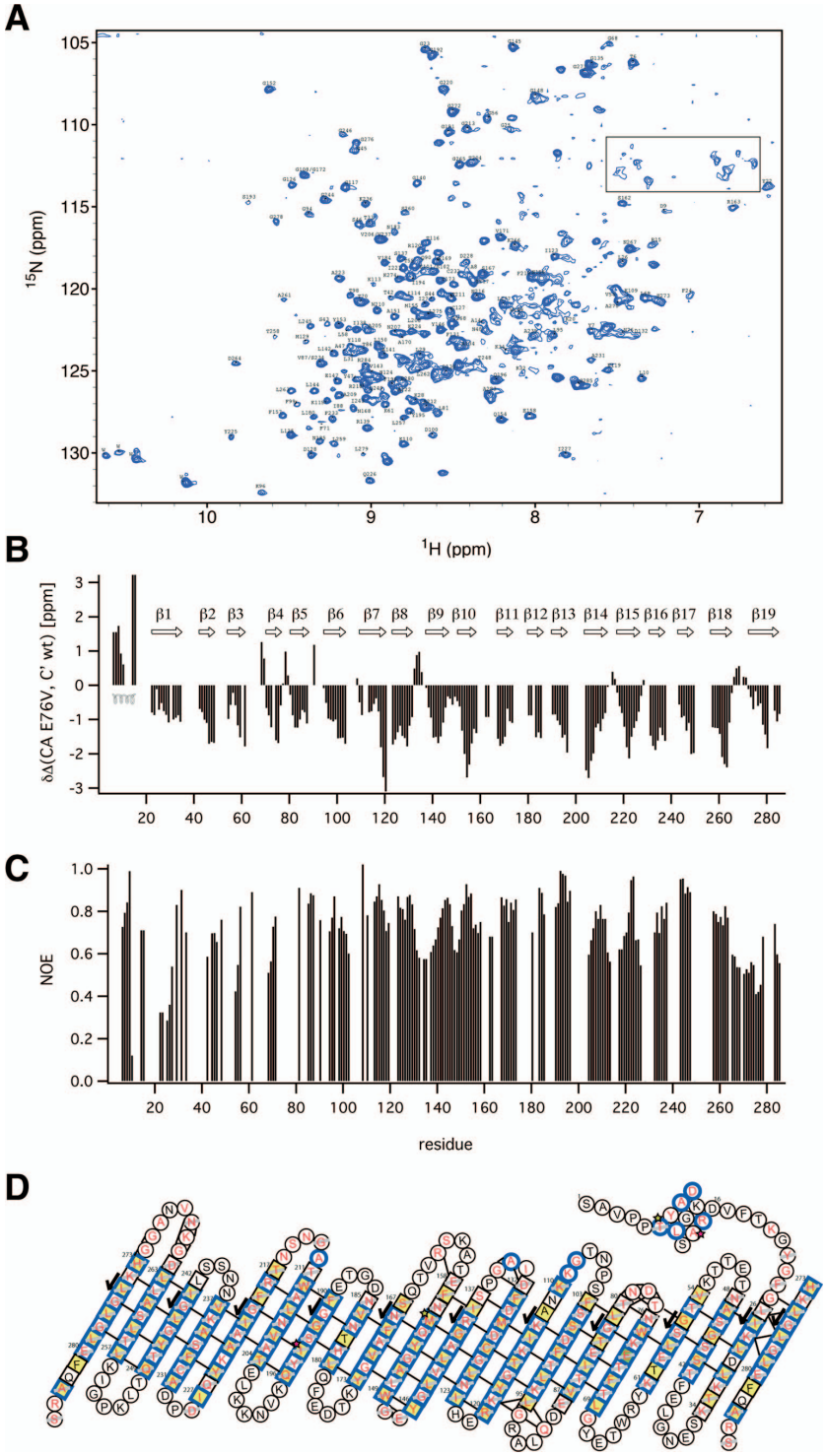

Fig. S1. Topology of hVDAC1. (*A*) ^{15}N-^{1}H TROSY spectrum of hVDAC1 measured at 900 MHz. Resonance assignments are indicated with residue numbers. A rectangle marks Gln and Asn side chain resonances. (*B*) Three-bond averaged Cα and C′ secondary chemical shifts, calculated as the difference between experimental chemical shifts observed for Cα in E73V and C′ in *wt* hVDAC1 and their respective random coil values. Secondary chemical shifts were averaged over a three-residue window. The 19 β-strands indicated by characteristic negative secondary chemical shifts are denoted by arrows with strand numbers above. (*C*) Heteronuclear ^{1}H-^{15}N NOEs of hVDAC1 measured at 900 MHz. Intensity ratios were averaged over a three-residue window. (*D*) Topology map of hVDAC1. β-strands identified on the basis of Cα and C′ secondary chemicals, slow amide proton exchange rates and HN-HN NOEs are boxed. Assigned residues are colored in red. Residues showing slow amide proton exchange in E73V hVDAC1 are indicated by blue boxes. Medium- and long-range HN-HN NOEs are indicated by black lines. Residues with negative Cα and C′ secondary chemical shifts are indicated by gray lines. β-strand residues with their side-chains facing the membrane are colored in yellow. Two weak HN-HN NOEs between the helix and the barrel, T6-M155 and A14-I194, are indicated by green and pink stars, respectively.

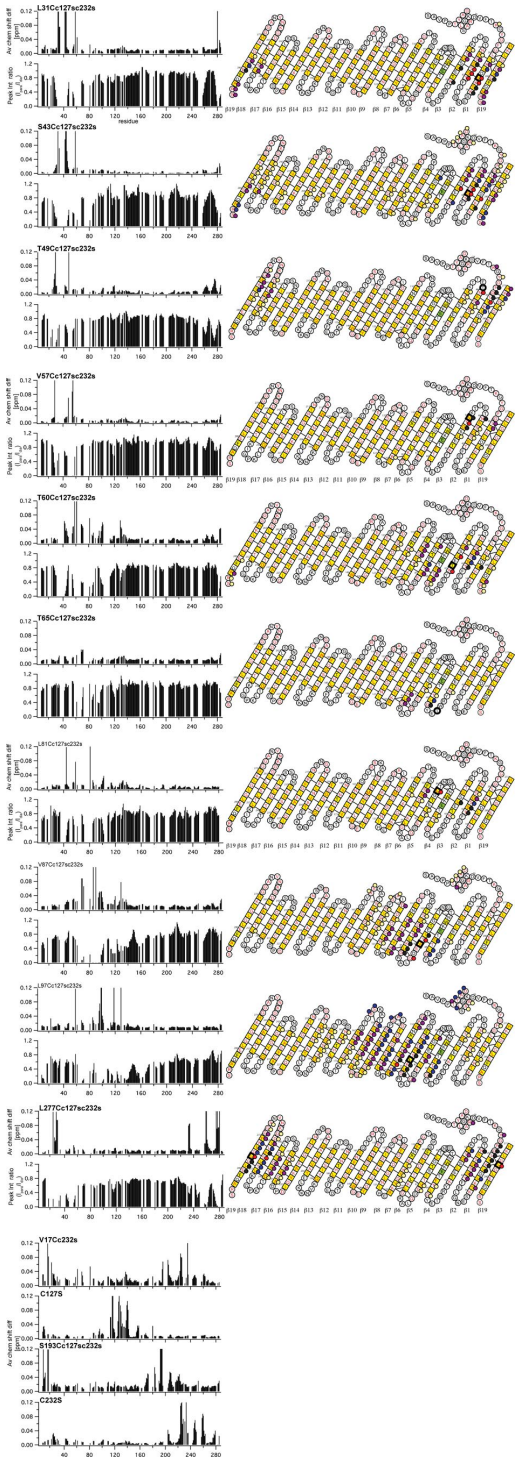

Fig. S2. Chemical shift changes and PRE data of mutants. For each mutant for which PRE data are present normalized weighted average $^{1}H/^{15}N$ chemical shift changes observed in $^{2}H/^{15}N$-labeled hVDAC1 upon mutation are shown in *Upper Left* and intensity ratios (I_{para}/I_{dia}) of crosspeaks in the $^{1}H/^{15}N$ TROSY-HSQC are shown in *Lower Left*. In *Right*, PRE data are mapped onto the topology map of hVDAC1. Residues which could not be reassigned in the mutant spectrum are labeled with a red dot, peaks which are broadened beyond detection, with a black dot. Peaks with an intensity ratio between 0 and 0.2 are labeled with a blue dot, between 0.2 and 0.4 with a purple dot and between 0.4 and 0.6 with a light yellow dot, respectively. In the topology map β-strands identified on the basis of Cα and C′ secondary chemicals, slow amide proton exchange rates and HN-HN NOEs are boxed. Assigned residues are colored in red. Medium- and long-range HN-HN NOEs are indicated by black lines. β-strand residues with their side-chains facing the membrane are colored in yellow. Mutation sites are bordered with bold black lines. Additionally normalized weighted average $^{1}H/^{15}N$ chemical shift changes observed in $^{2}H/^{15}N$-labeled hVDAC1 upon mutation are shown for selected mutants equally distributed over the C terminus of hVDAC1 and for one mutant in the helix. All data are averaged over a three-residue window. Chemical shift changes of triple and double mutants were calculated in reference to the corresponding double and single mutants, respectively.

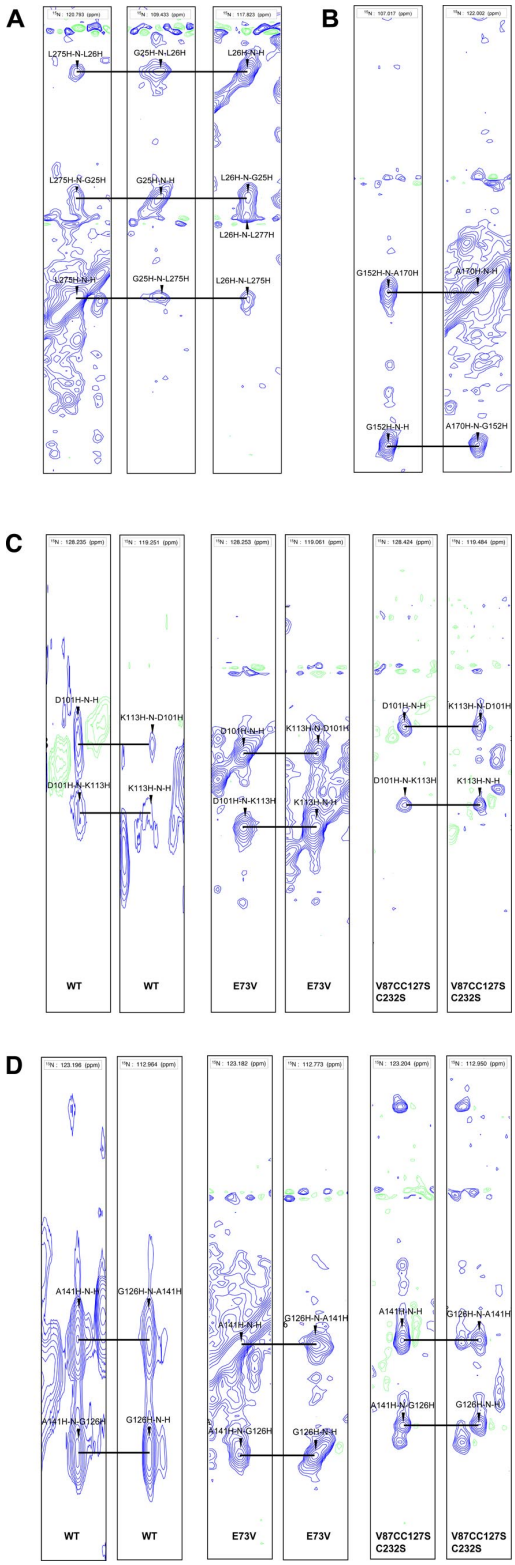

Fig. S3. NOE cross-peaks. (*A*, *B*) Strip plot of the 3D HMQC-NOESY spectrum of E73V hVDAC1 measured at 310 K and 800 MHz. Exemplarily, NOE crosspeaks defining (*A*) the parallel arrangement of β-strands β1 and β19 and (*B*) the antiparallel arrangement of β-strands β10 and β11 are shown. Residues are indicated with the one letter amino acid code and the corresponding atom name (H, N) after the corresponding residue number. (*C*, *D*) Strip plot of the 3D NOESY-HSQC of wild type hVDAC1 (WT) and the 3D HMQC-NOESY spectra of E73V and V87CC127SC232S hVDAC1 measured at 310 K and 900 MHz (WT) and 800 MHz (mutants). Exemplarily, NOE crosspeaks that shift upon the mutation are shown. Residues are indicated with the one letter amino acid code and the corresponding atom name (H, N) after the corresponding residue number.

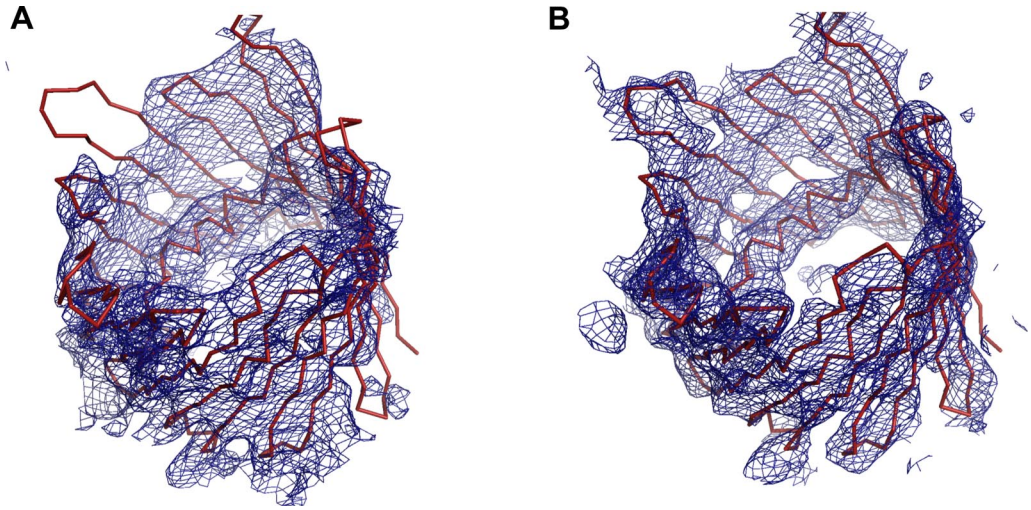

Fig. S4. Joint NMR/x-ray refinement. View of density contoured at 1 sigma. (*A*) Initial density after experimental phasing with SHARP and phase improvement through density modification with SOLOMON. (*B*) Final $2mF_o$-DF_c density from BUSTER-TNT.

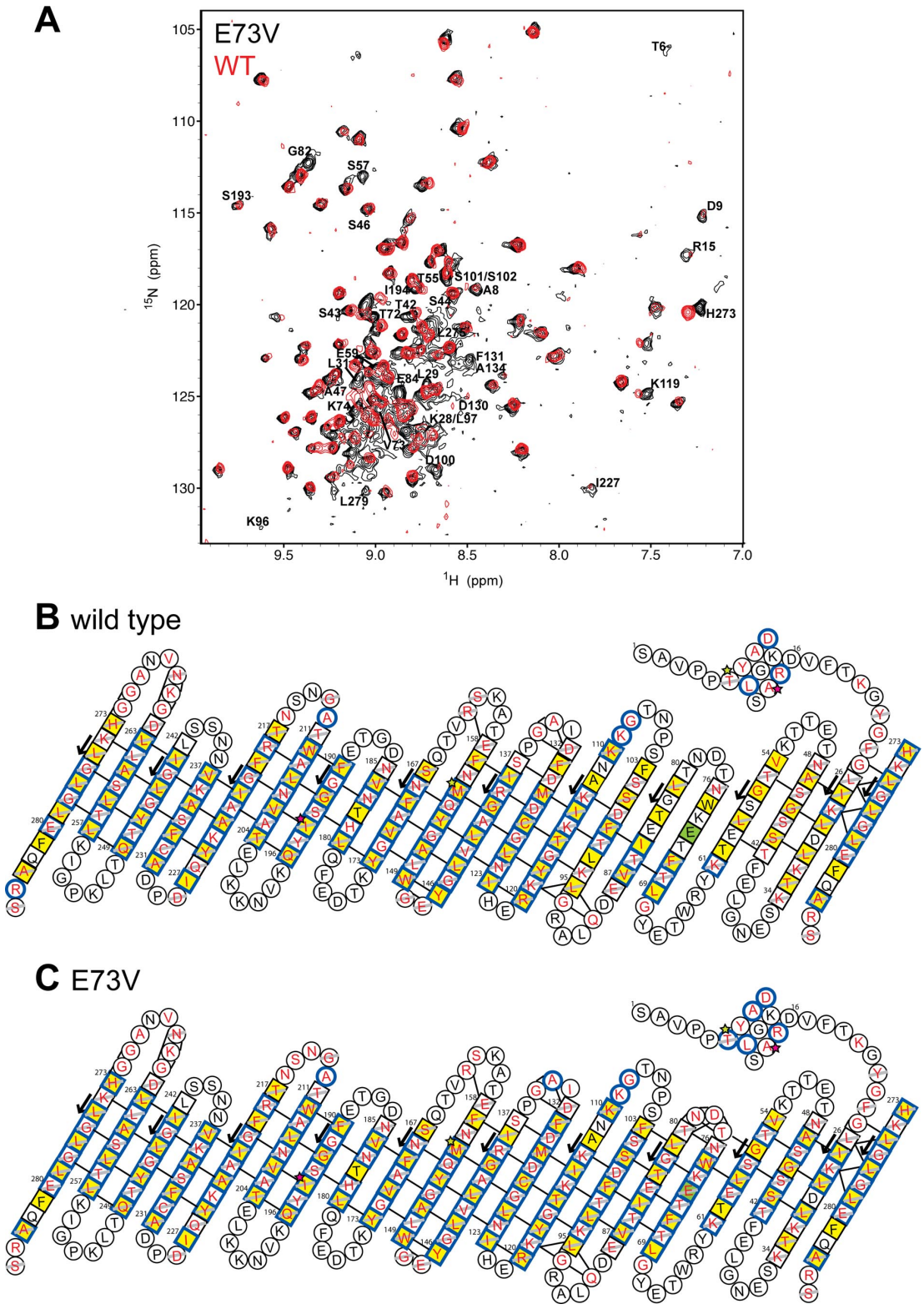

Fig. S5. Comparison of amide proton exchange, backbone resonance assignment and HN-HN NOEs in *wt* and E73V hVDAC1. (*A*) H/D exchange of *wt* (red) and E73V (black) hVDAC1 at 37°C as monitored by ^{15}N-^{1}H TROSY spectra. The NMR measurements were completed 2 hours after transfer of the proteins into 100% D_2O. Resonance assignments of residues with slow amide proton exchange in E73V hVDAC1 are indicated with residue numbers. (*B*, *C*) Topology map of WT (*B*) and E73V (*C*) hVDAC1. Residues in β-strands identified by NMR are boxed. Assigned residues are colored in red. Residues showing slow amide proton exchange are indicated by blue boxes. Medium- and long-range HN-HN NOEs are indicated by black lines. Residues with negative Cα secondary chemical shifts are indicated by gray lines. β-Strand residues with their side-chains facing the membrane are colored in yellow.

Table S1. List of NMR restraints that localized the N-terminal α-helix

NMR restrains that localize the helix	
NOEs within the helix	T6-Y7
	T6-A8
	T6-D9
	Y7-A8
	Y7-D9
	Y7-L10
	A8-D9
	A8-L10
	D9-L10
NOEs to the barrel	T6-M155
	A14-I194
Residues that shift upon the V17C mutation	Q196
	T204
	A205
	V206
	L208
	A223
	Y225
	Q226
	A235
	K252
	L259
	L262
Residues that shift upon the S193C mutation	D9
	L10
	A14
	R15
Residues that experience PRE broadening due to MTSL attached to C232	A14
	R15
	Y22
Residues that experience PRE broadening due to MTSL attached to L277C	T6
	R15
	Y22

Table S2. List of crystallographic data

Data collection statistics														
Dataset			TM77(SeMet)		TM10		PtV4(Pt)				TM7(SeMet)			
Wavelength	[Å]		0.97947		0.95370		1.07150		0.97950 (peak)		0.97970 (inflection)		0.97560 (remote)	
Unit cell dimensions			78.0 78.0 167.0		79.9 79.9 167.4		77.7 77.7 166.5		77.8 77.8 166.3		77.6 77.6 166.4		77.8 77.8 166.7	
Resolution range*	[Å]		43.0–4.1	(4.3–4.1)	43.4–4.2	(4.5–4.2)	35.4–5.8	(6.1–5.8)	42.8–4.3	(4.5–4.3)	42.8–4.3	(4.5–4.3)	42.8–4.3	(4.5–4.3)
Observations			82200	(5682)	58879	(5612)	11590	(650)	18815	(2284)	18315	(1565)	17578	(1122)
Unique reflections			4887	(688)	4747	(660)	1797	(214)	4361	(598)	4250	(445)	4129	(346)
Multiplicity			16.8	(8.3)	12.4	(8.5)	6.4	(3.0)	4.3	(3.8)	4.3	(3.5)	4.3	(3.2)
Completeness	[%]		99.5	(99.1)	99.8	(99.0)	96.8	(84.1)	98.3	(95.5)	98.5	(90.7)	98.2	(88.5)
R_{merge}	[%]		9.8	(54.0)	6.3	(50.6)	6.4	(40.1)	5.7	(51.0)	5.6	(55.4)	6.0	(53.5)
I/sig*I*			16.4	(3.5)	43.6	(3.5)	13.2	(2.3)	20.1	(2.1)	20.3	(1.9)	20.7	(1.7)
Phasing power (ano)		acen		0.53				0.45		0.73		0.54		0.42
Phasing power (iso)		acen/cen	0.13	0.09	0.26	0.14	0.85	0.57	-		0.21	0.24	0.16	0.16
f.o.m.		acen/cen			0.31						0.27			
Refinement statistics														
Resolution range	[Å]		25.0–4.1	4.3–4.1										
No. of reflections		all	4840	(689)										
		work	4363	(608)										
		test	477	(81)										
R-factor	[%]	all	33.1	(22.4)										
		work	32.5	(22.2)										
		test	38.7	(23.2)										
Protein atoms			2207											
Mean B-factor	[Å^2]		179.1											
rms(bond)	[Å]		0.003											
rms(angle)	[°]		0.621											

*Different datasets showed various degree of anisotropy. Following the criteria of Strong *et al*. (26) with a cutoff for *F*/sigma(F) of 4, dataset TM10 gives high-resolution limits in the three main directions (d1, d2, and d3) of 4.4, 4.4, and 4.1 Å (where the directions are defined as d3: perpendicular to a* and b*, d2: along b* and d1: perpendicular to b* and d3).

Table S3. Refinement R-factors vs. resolution

	R-factor		
Resolution	Work	Test	All
17.4	0.3612	0.4179	0.3683
10.0	0.3422	0.3539	0.3435
7.8	0.3447	0.4641	0.3561
6.6	0.3935	0.4915	0.4022
5.8	0.3576	0.5375	0.3720
5.2	0.3124	0.4085	0.3210
4.8	0.2556	0.2627	0.2562
4.5	0.2137	0.2747	0.2204
4.2	0.2223	0.2320	0.2235
Overall	0.3250	0.3873	0.3314